To be published in Applied Optics:

Title: Grating-assisted-cylindrical-resonant-cavities interlayer coupler
Authors: Congshan Wan,Thomas Gaylord,Muhannad Bakir
Accepted: 22 May 18
Posted 23 May 18
Doc. ID: 325562

Grating-assisted-cylindrical-resonant-cavities interlayer coupler

CONGSHAN WAN[1*], THOMAS K. GAYLORD[1], AND MUHANNAD S. BAKIR[1]

[1] School of Electrical and Computer Engineering, Georgia Institute of Technology, Atlanta, Georgia 30332, USA
[*] Corresponding author: cwan3@gatech.edu

Compiled May 22, 2018

A grating-assisted-cylindrical-resonant-cavities (GARC) interlayer coupler made of Si/SiO_2 is designed and simulated to achieve efficient and broadband interlayer coupling. This coupler consists of three cylindrical resonant cavities: two waveguide cavities in the horizontal direction and one cylindrical via cavity in the vertical direction. The resonant strengths of the two cylindrical waveguide cavities are enhanced by circular Bessel-function-defined gratings and distributed Bragg reflectors. The interlayer coupling efficiency of this Si/SiO_2 GARC coupler is simulated as η_c = 68% (-1.7 dB) for TE polarization at 1.55 μm wavelength, which is generally higher than those of conventional rectangular SOI gratings with additional features such as reflectors, overlayers, chirped periods, dual-gratings, etc. The GARC couplers are predicted to have favorable attributes compared with previous couplers including wider operational bandwidth ($\delta_{\lambda,1dB}$ = 270 nm), larger tolerance to in-plane misalignment ($\pm$2 μm for 1 dB extra loss), easier grating patterning (wider grating ridges), smaller footprint (20 μm in diameter), and more flexible choices of interlayer distances (2 $\sim$ 5 μm). A sensitivity analysis is also provided as a guide in fabrication. In general, it is found that the vertical dimensions of the GARC couplers need to be carefully controlled while the horizontal dimensions are less critical.

OCIS codes: (050.2770) Gratings; (060.1810) Couplers; (130.0130) Integrated optics; (130.2790) Guided wave; (250.5300) Photonic integrated circuits; (260.5740) Resonance; (310.4165) Multilayer design.

http://dx.doi.org/10.1364/ao.XX.XXXXXX

1. INTRODUCTION

2.5D and 3D IC integration technologies [1, 2] have become increasingly important in the fields of high-performance computing [3], parallel image processing [4], and 5G wireless communication [5], etc. The use of optical links together with the electrical links provides promising solutions to increase signal bandwidth and reduce power consumptions. The emergence of 3D integrated photonics [6] offers opportunities for denser and more complex network designs without the problems of waveguide crossings and crosstalk. The successful demonstration of 3D photonics relies on the performance of interlayer optical couplers, and thus designing high-efficiency interlayer couplers becomes an unavoidable task. Conventionally, the interlayer optical connectivity is achieved by using 45° mirrors, evanescent couplers, or diffraction gratings. One- or two-dimensional rectangular waveguide gratings have been extensively studied to date because they can achieve relatively large interlayer distances and their planar geometries make them compatible with IC wafer-scale fabrication and testing. Increasing the diffraction efficiencies of rectangular gratings is essential to reduce the coupling loss, and the most effective approaches have been choosing materials with large refractive index contrast (e.g. SOI) and engineering the grating period, etch depth, and fill factor [7], which fundamentally change the diffraction behavior. However, further efficiency improvement into the desired diffraction direction continues to be a challenge due to the presence of substrate leakage loss, back-reflection, and forward-transmission (Fig. 1). These problems have been mitigated by applying poly-Si overlayers (to enhance directionality) [8–10], asymmetric profiles (to enhance directionality) [11], DBR or metal reflectors (to reduce substrate leakage) [12–16], apodized or chirped gratings (to reduce back-reflection) [17], in-plane grating reflectors (to reduce forward-transmission) [18, 19], dual-grating layer [20, 21], and novel subwavelength structures [22–28]. Some reported rectangular SOI gratings are summarized in Table 1. It is observed that narrow grating ridges ($\sim$100 nm) are required to achieve relatively high efficiencies (>70%), and such gratings can only be patterned using high-resolution fabrication techniques, e.g. e-beam lithography. The methods used to increase the directionality, e.g. depositing overlayers or applying reflectors, also add complexity to the fabrication process. Apart from the fabrication difficulties, grating assembly poses additional challenges to pho-

tonics integration and packaging processes because rectangular grating couplers are very sensitive to misalignments [29]. All of these issues, regarding resolution, directionality, and misalignment, originate from the Floquet and Bragg conditions which rectangular gratings must inherently follow.

In the present work, we are proposing a fundamentally different approach, the Si/SiO_2 grating-assisted-cylindrical-resonant-cavities (GARC) interlayer coupler, to achieve efficient and broadband interlayer coupling. The previous Si_3N_4/SiO_2 coupler reported in [30] consists of a pair of circular gratings together with a high-index via. In this work, we further develop this concept and provide a new Si/SiO_2-based design. The high-index via plays a significant role as a cylindrical resonant cavity in the vertical direction, and the GARC coupler thus benefits from the large increase of the resonant optical field introduced by the cavity. In addition, the outer circular gratings serve as distributed Bragg reflectors (DBR), forming another set of resonant cavities in the horizontal direction and enhancing the fields which are modulated by the inner circular gratings. Field transport between waveguides and the via is achieved based on evanescent coupling. Since the circular gratings are defined by the in-plane interference instead of the Floquet condition of rectangular gratings, relatively wide grating ridges can be used. Furthermore, it is not necessary to incorporate adjacent-layer reflectors because there are no propagating fields in the substrate. At 1.55 μm wavelength, the simulated interlayer coupling efficiency η_c for an optimized Si/SiO_2 GARC coupler is 68% by using a range of resolutions (see Appendix A). For a general perspective on coupling performance of existing SOI rectangular grating couplers, Table 1 is presented. These results are typically obtained from 2D simulations. Figure 2 shows values of a number of key parameters as they have developed over time. It is observed that the GARC coupler has a relatively high efficiency, a very wide bandwidth, and a large minimum feature size. The most significant benefit of the GARC coupler is perhaps the wide spectral bandwidth ($\delta_{\lambda,1dB}$ = 270 nm), which can't be achieved by conventional rectangular gratings. The GARC couplers also demonstrate many advantages such as CMOS compatible fabrication, flexible choices of interlayer separation, and high misalignment tolerances. To the best of the authors' knowledge, this is the first treatment of combining circular resonators in both horizontal and vertical directions to achieve interlayer coupling. Here we discuss material selection, design optimization, and sensitivity analysis.

2. OPTIMIZED SI/SIO$_2$ GARC COUPLER

Figure 3 shows the GARC coupler in which relatively high-index waveguides and a via are configured to couple optical signals between layers otherwise separated by an air gap. This structure can be implemented between two separate overlaid chips or embedded within an interconnected stack of chips. In the second case, the air gap can be filled with SiO_2, which will cause only small changes to the overall design. Transverse electric (TE) polarization (H_z, H_r, H_θ, E_r, E_θ) is considered for demonstration. GARC couplers for the transverse magnetic (TM) polarization (E_z, E_r, E_θ, H_r, H_θ) follow the same design process except that the TM guided-mode propagation constant β is used and relative permittivity is introduced to determine the grating ridges; e.g. for a 0.22 μm thick air/Si/SiO_2 waveguide, β = 11.371 μm^{-1} for the TE polarization whereas β = 7.5996 μm^{-1} for the TM polarization. For the TE polarization, the E_θ field in the circular slab waveguide is of primary importance because it is tangent

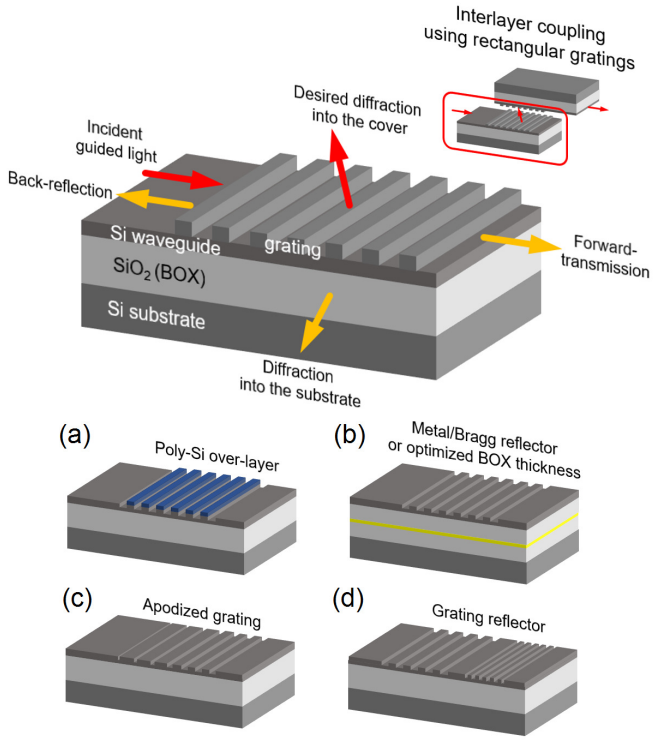

Fig. 1. Rectangular gratings used for interlayer coupling and possible solutions to reduce losses in binary SOI grating out-couplers: (a)(b) increasing directionality to cover, (c) reducing back-reflection, and (d) reducing forward-transmission.

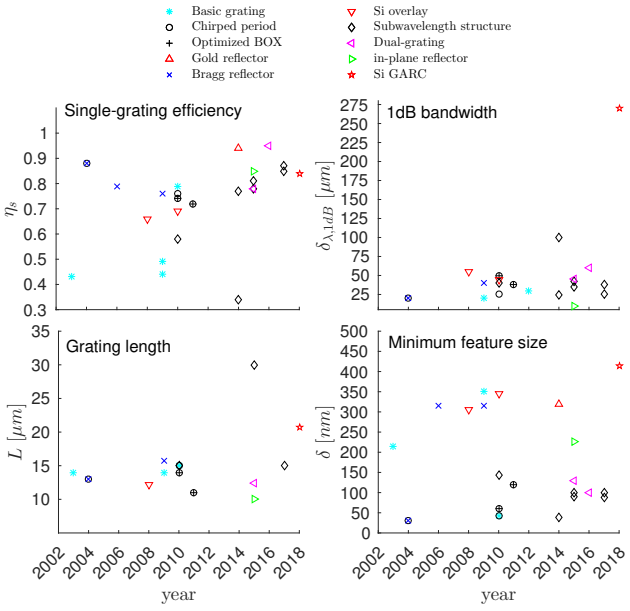

Fig. 2. Summary of single-grating efficiency η_s, 1dB bandwidth $\delta_{\lambda,1dB}$, grating footprint (L) and minimum feature size (δ) of SOI rectangular gratings reported in [8–10, 12–28, 31–34] as well as those for the Si/SiO_2 GARC coupler.

Table 1. Some reported SOI gratings for TE polarization. All references except [16] describe fiber-to-grating couplers. The column labels represent Si waveguide thickness (t_{Si}), grating period (Λ), grating etch depth (t_g), grating fill factor (F), grating line resolution (δ), grating length or dimension (L), single-grating efficiency (η_s), working wavelength (λ), and 1dB or 3dB bandwidth (1dB/3dB). CP, AP and DE represent chirped grating period, apodized fill factor, and double etch depths/widths, respectively.

SOI Structure						Measurement			Simulation			Reference
t_{Si} (nm)	Λ (nm)	t_g (nm)	F	δ (nm)	L (μm)	η_s (%/dB)	λ (nm)	1dB/3dB (nm)	η_s (%/dB)	λ (nm)	1dB/3dB (nm)	and Comments
340	CP	200	AP	43	15	75.8/-1.2	1533	–/45	79/-1.0	1550	–/48	[17]
340	630	340	0.85	95	10	44/-3.6	1560	–/50	–	–	–	[31]
220	701	220	0.5	350	14	–	–	–	49/-3.1	1550	20/35	[32]
220	632	70	–	–	–	25/-6	1560	30/–	–	1550	30/60	[33]
380	430	70	0.5	215	14	43/-3.7	1310	–	–	–	–	[34]
220	CP	220	AP	120	11	35/-4.6	1536	47/–	72/-1.4	1550	38/–	[35] [a]
250	CP	–	AP	60	14	64/-1.9	1524	42/70	74/-1.3	1520	50/80	[36] [a]
220	640	70	0.5	320	12.8	91/-0.41	1590	–	94/-0.28 [b]	1550	–	[16] [b, c]
220	630	70	0.5	315	15.75	69.5/-1.6	1520	36/63	76/-1.2	1550	40/60	[13] [d]
220	CP	100	AP	30	13	–	–	–	88/-0.6	1550	–/40	[14] [d]
220	630	70	0.5	315	–	–	–	–	79/-1.0	1550	–	[15] [d]
220	610	70	0.5	305	12.2	55/-2.6	1530	50/–	66/-1.8	1550	55/–	[8] [e]
220	690	70	0.5	345	–	69/-1.6	1530	44/80	–	–	–	[10] [e]
220	568	DE	AP	100	–	65/-1.9	1310	23/–	85/-0.7	1310	25/–	[22] [f]
220	780	DE	DE	100	30	74/-1.3	1550	–/52	78/-1.1	1550	35/50	[23] [f]
220	663	DE	AP	87	15	71/-1.5	1533	–/49	87/-0.6	1550	38/50	[24] [f]
220	–	220	–	39	40	23/-6.4	1550	100/–	34/ -4.7	1550	100/–	[26] [f]
200	–	DE	0.5	–	15	–	–	–	77/-1.1	1550	24/ –	[28] [f]
300	565	150	0.77	130	12.4	–	–	–	78/-1.1	1550	–/65	[20] [g]
120	–	–	–	–	–	92/-0.36	1197	–	95/-0.2	1200	–/100	[21] [g]
250	420	250	0.54	227	10	–	–	–	85.3/0.69	1310	–/20	[19] [h]

[a] Optimized BOX layer thickness [b] Interlayer grating coupler [c] Gold reflector [d] Bragg reflector [e] Poly-Si overlay
[f] Subwavelength structure [g] Dual-grating layer [h] In-plane reflector [i] Si_3N_4 waveguide [j] Si_3N_4/SiO_2 coupler

to the cylindrical wavefronts whose interference will determine the grating ridges. In the limiting case where the radius of the circular slab is infinite, the cylindrical wavefront becomes planar and the E_θ field can be treated as the E_y field of a typical rectangular slab waveguide that supports TE modes (E_y, H_x, and H_z). The necessity of the via, which is used for evanescent coupling, and the definition of the circular grating, which is based on the interference conditions, are explained in our previous work [30].

Figure 4 shows the cross-sectional views of the optimized Si/SiO_2 GARC coupler. The parameters indicated in Fig. 3 for the optimized GARC are summarized in Table 2. Full-wave simulations were performed using MEEP 3D FDTD [37]. A TE-polarized Gaussian pulse with free-space wavelength 1.55 μm and temporal width 33 fs is launched into the fundamental mode from the top slab waveguide and 68% of the input power is coupled into the bottom slab waveguide (η_c = 68%, which is calculated as the ratio of the output power from the GARC coupled into the bottom waveguide to the corresponding output power from a uniform waveguide without the GARC). The single-layer efficiency of GARC is approximated as $\eta_s = \sqrt{\eta_c} = 82\%$. The via and waveguides are made of Si. The grating is etched into the Si circular waveguide and filled with SiO_2. The low-index layer, made of SiO_2, is sandwiched between the grating and the via. Note that the stacking sequence is different from that of the Si_3N_4/SiO_2 GARC coupler [30], in which the grating is etched into the via and the low-index layer is located between the waveguide and the grating. The stacking sequence depends on the longitudinal field distribution in the waveguide. In the Si/SiO_2 waveguide, the refractive index contrast is larger and the longitudinal field is more confined in the waveguide core, leaving a short evanescent tail in the cladding or the low-index layer. In order to perturb the field in the circular waveguide, the grating needs to be etched into the waveguide. The etch depth should be shallow to reduce back-reflection into the input

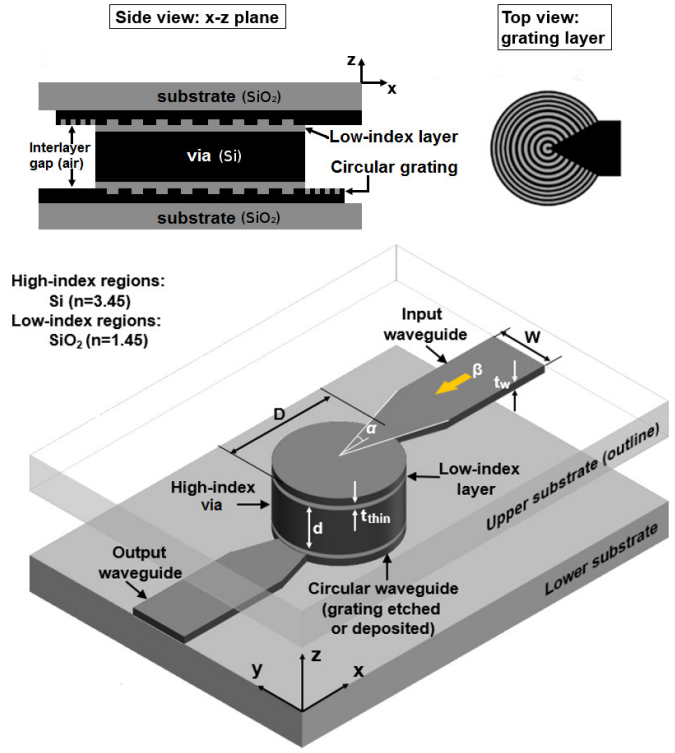

Fig. 3. Schematic representation of the GARC coupling configuration. The GARC structure functions to interconnect two layers otherwise separated by an air gap.

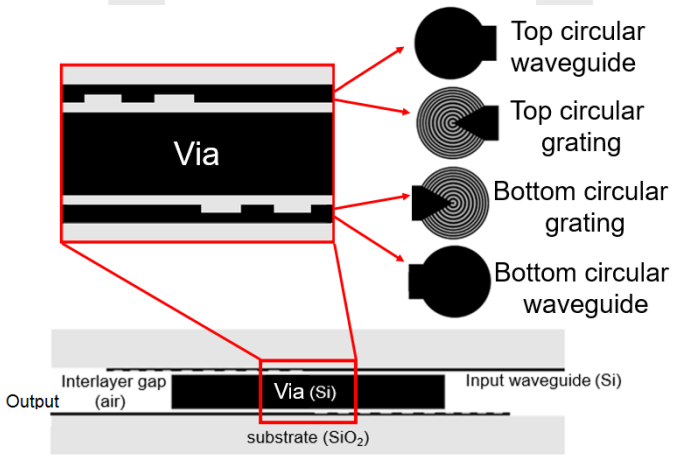

Fig. 4. Cross-sectional views of the Si/SiO_2 GARC coupler.

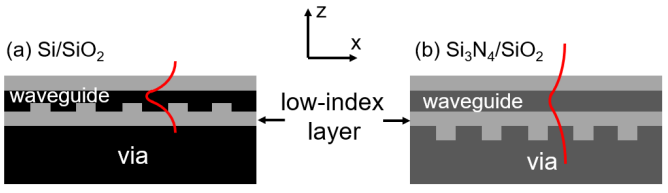

Fig. 5. Layer stacking sequence and longitudinal field distribution in two types of GARC couplers: (a) Si/SiO_2 and (b) Si_3N_4/SiO_2. Darker color indicates higher index.

Table 2. Parameters for the optimized Si/SiO_2 GARC coupler.

Inner and Outer Circular Grating Ridge Edges					
l	ω_l [a]	r [b] (μm)	w_r [c] (μm)	w_v [d] (μm)	Λ [e] (μm)
1	1.8412	0.3238	0.3238	–	–
2	5.3314	0.9377	–	0.6139	–
3	8.5363	1.5014	0.5637	–	1.1776
4	11.7060	2.0589	–	0.5575	–
5	14.8636	2.6143	0.5554	–	1.1129
6	18.0155	3.1687	–	0.5544	–
7	21.1644	3.7225	0.5538	–	1.1082
8	24.3113	4.2760	–	0.5535	–
9	27.4571	4.8293	0.5533	–	1.1068
10	30.6019	5.3824	–	0.5531	–
11	33.7462	5.9355	0.5530	–	1.1061
12	36.8900	6.4884	–	0.5530	–
13	40.0334	7.0413	0.5529	–	1.1059
14	43.1766	7.4559	–	0.4146	–
15	46.3196	7.8706	0.4146	–	0.8292
16	49.4624	8.2851	–	0.4146	–
17	52.6050	8.6997	0.4146	–	0.8292
18	55.7476	9.1142	–	0.4145	–
19	58.8900	9.5288	0.4145	–	0.8290
20	62.0323	9.9433	–	0.4145	–
21	65.1746	10.3578	0.4145	–	0.8290
Other Parameters					
β [f] (μm^{-1})	11.37	λ [g] (μm)	1.55		
k_0 (μm^{-1})	4.05	n_{SiO_2} [h]	1.45		
n_{Si} [h]	3.45	γ_{Si} [i] (μm^{-1})	8.12		
t_w (μm)	0.22	t_g (μm)	0.04		
t_{thin} (μm)	0.1	W (μm)	10		
ϕ (°)	35.5	α (°)	28.65		
D_{inner} [j] (μm)	14.08	D_{outer} [j] (μm)	20.72		
p, s, t [k]	2, 3, 2	d (μm)	2		

[a] lth zero of $J_1'(x) = d[J_1(x)]/dx$; [b] Location of grating ridge edges as shown in Fig. 6; [c] Grating ridge width; [d] Grating groove width; [e] Local grating period; [f] radial (r) propagation constant; [g] free-space wavelength; [h] n represents refractive index; [i] longitudinal (z) propagation constant; [j] Inner and outer grating diameters; [k] parameters used to define circular grating ridges [30].

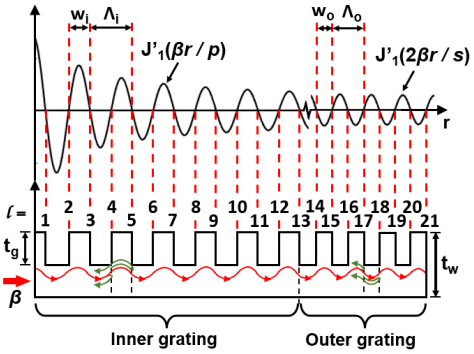

Fig. 6. Circular grating ridge definition. Corresponding parameters are shown in Table 2.

taper. By contrast, the index difference is small in a Si_3N_4/SiO_2 waveguide and thus the longitudinal field extends further out of the waveguide core. A grating layer adjacent to the waveguide is sufficient to perturb the field, while an etched grating may induce too much back-reflection. This difference is illustrated in Fig. 5. The efficiency has increased from 41% for the Si_3N_4/SiO_2 coupler to 68% for the Si/SiO_2 coupler due to a stronger field confinement in the Si via.

As shown in Fig. 6, the circular grating ridges are defined by using $p = 2$, $s = 3$ and $t = 2$ according to [30]. The minimum grating ridge widths of the optimized Si/SiO_2 GARC coupler is 553 nm (Λ_{inner} = 1.106 μm) for the inner grating and 415 nm (Λ_{outer} = 830 nm) for the outer grating. If the parameters $p = s = t = 1$ are used, the inner and outer grating ridge widths will be 276 nm and 138 nm, respectively, which would be more difficult to photo-define. The grating ridge widths can be further increased by using larger integer values of p, s and t if the coupler footprint permits. The flexibility to define circular gratings based on the interference conditions circumvents the difficulty of writing narrow grating ridges which are inevitable in traditional rectangular gratings. The grating etch depth is 40 nm, which has been optimized using parameter sweeps.

As discussed in [30], the circular grating is defined according to the Bessel function $J_1(\beta r)$ [38, 39], whose oscillation period is larger near the origin and becomes smaller at larger radial distances r. However, at large argument r, $J_1(\beta r)$ can be approximated as $cos(\beta r)$, which is periodic. The inner circular grating (smaller r) should strictly follow the Bessel function $J_1(\beta r)$, but the outer circular grating (larger r) can be treated as periodic and defined according to $cos(\beta r)$. This can be observed from Table 2 where the period Λ is more uniform for the outer circular grating. This phenomenon will become more obvious when the circular grating is larger, e.g. the Si_3N_4/SiO_2 coupler in [30]. The method to define circular grating based on Bessel functions does not contradict common circular grating designs used as laser cavities, e.g. [40–42], etc., in which strictly periodic circular gratings are used. For example, in [40], the laser cavity consists of a uniform disk in the center (radius 5 μm) surrounded by circular Bragg reflector (from r = 5 μm to 60 μm). The central disk, where the pump medium is located, circumvents the necessity of grating definition, while the radial locations for the circular Bragg gratings are large enough such that the gratings can be treated as periodic.

The diameter of the inner circular grating D_{inner}, the width of the rectangular slab waveguide W, and the taper half-angle α

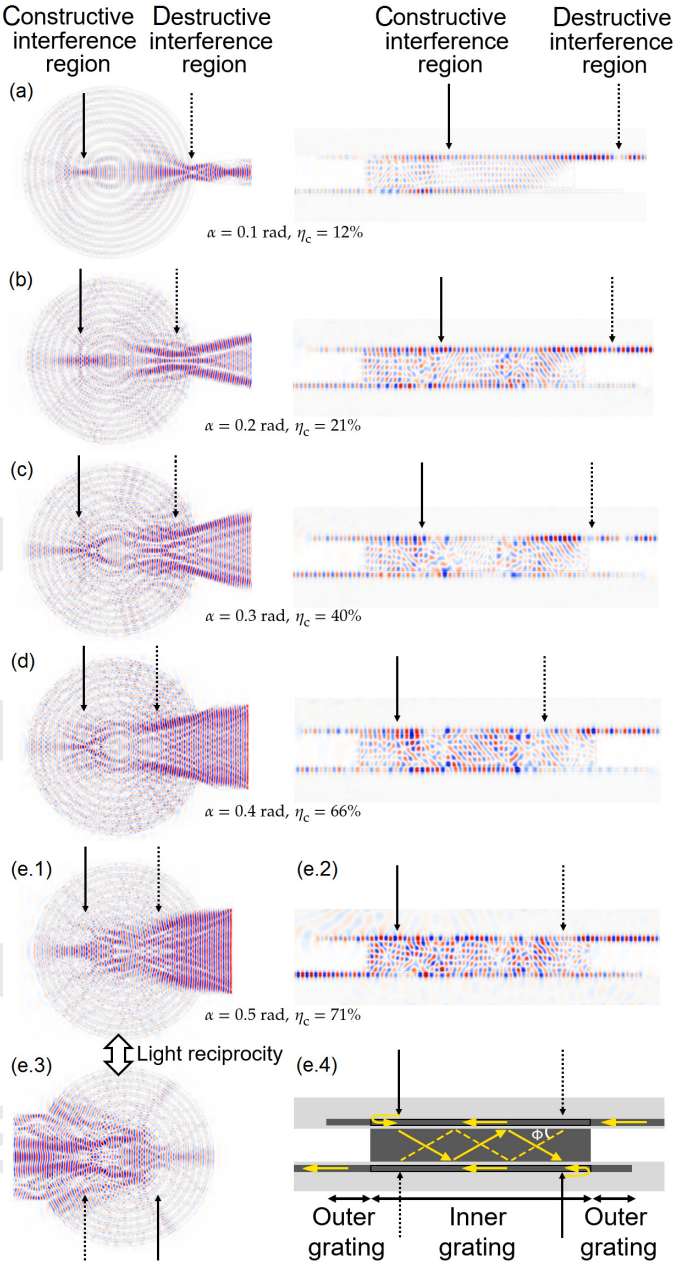

Fig. 7. The H_z field distribution in the top grating and in the vertical cross-section of the GARC coupler with five different taper half-angles: (a) 0.1 rad = 5.73°, (b) 0.2 rad = 11.46°, (c) 0.3 rad = 17.19°, (d) 0.4 rad = 22.92°, and (e) 0.5 rad = 28.65°. For case (e), the H_z field distribution in the bottom grating is shown in (e.3), and the ray representation of the vertical resonator in the via is shown in (e.4).

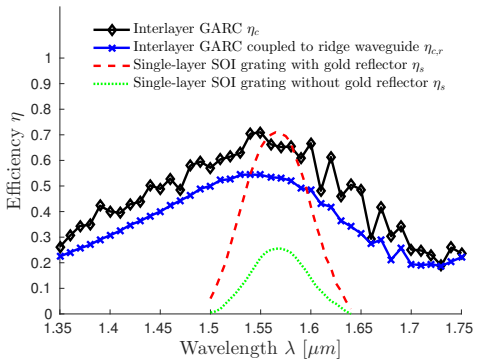

Fig. 8. Spectral response for the optimized Si/SiO_2 GARC coupler and the rectangular grating reported in [43].

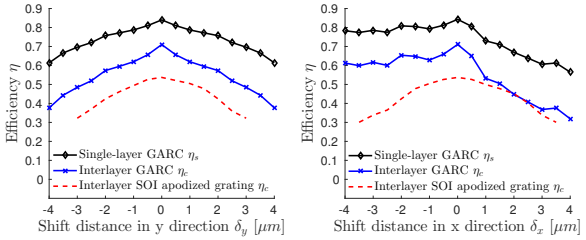

Fig. 9. Effect of translational shift in the y direction (a) and the x direction (b) for the optimized Si/SiO_2 GARC coupler specified in Table 2 and that of an apodized SOI grating coupler reported in [44].

affect the determination of the via height d or equivalently, the interlayer separation. The via diameter is the same as D_{inner}. Figure 7 shows the H_z field of the GARC coupler with five different taper half-angles. The angle 0.5 rad is the limiting case in which the taper side length equals $R_{outer} = D_{outer}/2$. The parameters $d = 2\ \mu m$, $D_{inner} = 14.08\ \mu m$, and $W = 10\ \mu m$ are the same for all cases. The smaller the taper half-angle, the longer the input taper (the entire taper is not shown for $\alpha = 0.1\ rad$ to $0.3\ rad$). It is observed that the "destructive interference region (DIR)" (indicated by the dashed arrow), the null field in the input taper due to destructive interference of input field and back-reflected field, moves inwards from the outskirts of the circular grating as taper half-angle increases. Once the input field reaches the inner grating, the field will be evanescently coupled to the high-index via and propagate at the angle $\phi = tan^{-1}(\gamma_{Si}/\beta) = 35.5°$. Note that not all of the field is coupled into the via; instead, a portion of the input field still propagates in the slab waveguide with an approximately exponential-decaying intensity due to the presence of the low-index layer. The obliquely propagating field in the via will be reflected from the bottom circular grating and then obliquely propagate upward with the angle $\pi - \phi$. Eventually, most of the reflected field will constructively interfere at the top grating, forming a "constructive interference region (CIR)" indicated by the solid arrow. It is desired that the CIR and DIR be located symmetrically about the grating center and both regions be located within the inner grating, e.g. Fig. 7 (e.1). This symmetry ensures that another set of CIR and DIR, whose locations are interchanged, are formed at the bottom grating, e.g. Fig. 7 (e.3). In other words, inversion symmetry about the center of the via has been achieved and the structure exhibits reciprocal behavior. Thus, α and W determine the location of the DIR; D_{inner} restricts the location of the CIR and DIR; and d controls the location of the CIR and the effectiveness of the vertical resonator.

The spectral response of the optimized Si/SiO_2 GARC coupler specified in Table 2 is shown in Fig. 8. Higher-order modes in the transverse direction (xy plane) will typically be excited in the slab waveguide, (which is also true for the slab waveguides connected to rectangular gratings). To suppress the higher-order modes in the transverse direction, waveguide tapers can be added to gradually narrow the width (W) of the the slab waveguide down to that of the ridge waveguides (W_r). This is particularly important in photonic circuits that use ridge waveguides which are evanescently coupled to ring resonators or to interferometers, etc. To suppress the higher-order modes in the output slab waveguide of the GARC, a waveguide taper with taper half angle 0.1 rad can be used to couple the slab modes into a ridge waveguide with width 0.5 μm (Fig. 19 in Appendix), and the resulting spectral response curve has correspondingly less oscillations and reduced efficiency due to the removal of higher-order modes. The coupling efficiency could be further improved by optimizing the taper angle and length. This has not been done in the present work. Since rectangular gratings are typically analyzed using 2D simulation (infinite in the y direction), those efficiency calculations do not include this tapering effect. Nevertheless the efficiency of the GARC remains relatively high even if a taper is included ($\eta_c = 55\%$, $\eta_s = 74\%$ at $1.55\mu m$). Compared with traditional rectangular grating couplers [43], the spectral bandwidth δ_λ of the GARC coupler is much wider. The 1 dB bandwidth for η_s and η_c of the GARC coupler are about 270 nm (for $\eta_s > 0.67$) and 170 nm (for $\eta_c > 0.57$), respectively. The quality factor can also be approximated from the spectral response as $Q = \lambda_c/\delta_{\lambda,3dB} = 1.55/0.3 = 5.2$, where $\delta_{\lambda,3dB} = 300\ nm$ indicates the 3 dB bandwidth or FWHM. Due to the field leakage into the waveguides, the via cavity is not a strong resonator but it still provides field enhancement.

3. SENSITIVITY ANALYSIS

The optimized couplers may not be fabricated and assembled precisely as designed. Using 3D FDTD, we have analyzed the effects of translational misalignments, layer thickness changes (e.g. grating etch depth, via height, etc.), grating ridge variations, and via taperings.

Figure 9(a) shows the effect of translational shift of the bottom waveguide with respect to the via in the y direction (the axes are shown in Fig. 3), assuming the circular gratings are exactly defined in the circular waveguides on both layers and the top circular waveguide is exactly aligned to the via. Since the GARC coupler is symmetric about the xz plane, the efficiency changes for the positive and negative shifts are identical. A misalignment tolerance of $\pm 2\ \mu m$ causes about 1 dB excess loss for the the GARC interlayer coupling efficiency, which is about the same amount of tolerance as for an SOI apodized grating coupler reported in [44]. The effect of shift in x direction is shown in Fig. 9(b). Shifting in the positive x direction has a larger effect on the efficiency than shifting in the negative x direction, which can be explained with the illustration in Fig. 10. The shaded yellow region indicates a relatively high power region in the via. When the bottom waveguide is shifted in the -x direction, high-power region and low-power region on the bottom waveguide

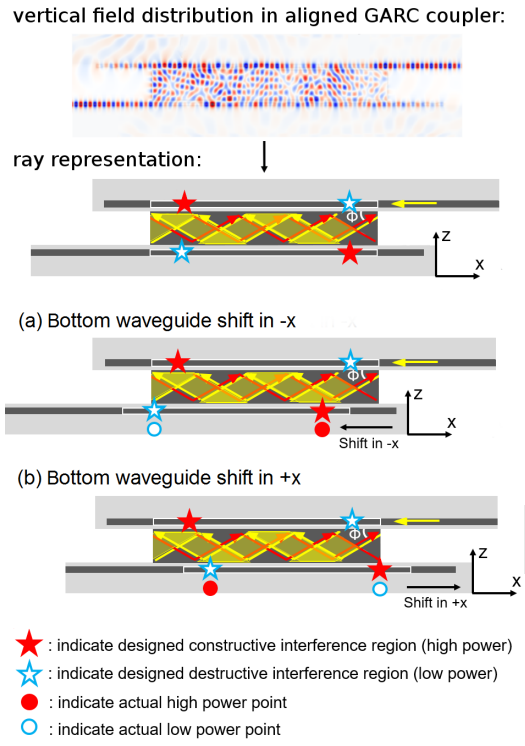

Fig. 10. Effect of translational shift in the x direction on the coupler performance.

are approximately located at the pre-designed CIR and DIR, respectively. By contrast, the high-power region and low-power region interchange their locations when the bottom waveguide is shifted in the $+x$ direction, which violates the light reciprocity and thus induces a relatively larger power loss. Rotational misalignment, which is particularly detrimental to the rectangular gratings, is not likely to occur in the GARC structure due to the presence of the via which offers a mechanical support between layers.

The effect of varying via height d on the GARC coupler efficiency is shown in Fig. 11. It is observed that the efficiency is sensitive to via height changes. Nevertheless, the layer thickness could be closely controlled during the deposition process and

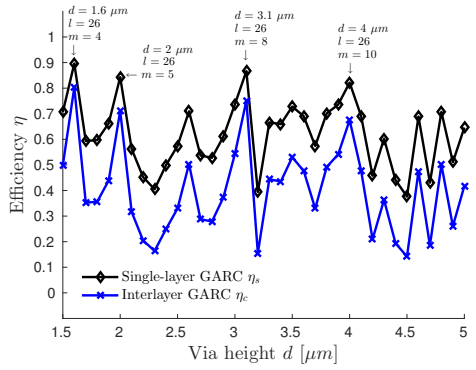

Fig. 11. Plot of efficiency as a function of via height.

Table 3. Resulting via height d in μm for the (l,m)-th resonance at 1.55 μm free-space wavelength (R = 7.0413 μm).

m \ l	24	25	**26**	27	28
4	1.3801	1.4682	**1.5807**	1.7302	1.9413
5	1.7251	1.8353	**1.9758**	2.1627	2.4266
6	2.0701	2.2023	2.3710	2.5952	2.9119
7	2.4151	2.5694	2.7662	3.0278	3.3972
8	2.7602	2.9364	**3.1613**	3.4603	3.8825
9	3.1052	3.3035	3.5565	3.8929	4.3678
10	3.4502	3.6705	**3.9516**	4.3254	4.8531

the optimal via height could be achieved without significant difficulty. Since the via functions as a cylindrical resonant cavity, the resonant wavelengths in the via are [45]

$$\lambda_{lm} = \frac{2\pi}{\sqrt{\left(\frac{\omega_l}{R}\right)^2 + \left(\frac{m\pi}{d}\right)^2}}, \tag{1}$$

where l and m indicate the resonant mode order in the radial (r) and longitudinal (z) directions, respectively, ω_l is the lth zero of the function $J_1'(x)$, R = 7.0413 μm is the radius of the via, and d is the via height. Since the GARC coupler is designed for the free-space wavelength λ = 1.55 μm, the resonance wavelength in the Si via is $\lambda_{lm} = \lambda/n_{Si}$, which can be achieved using various sets of l, m, and d. The via height d at the (l,m)-th resonance can be found from Eq. (1), and some results are shown in Table 3. Since the radius of the cylindrical cavity is fixed at R = 7.0413 μm, the resonance mode order l in the radial direction can be approximated as

$$R = \frac{l}{2}\lambda_r, \tag{2}$$

where λ_r is the radial component of λ_{lm} ($\lambda_r = 2\pi/\beta$ = 0.5526 μm). Thus l is approximated as 26, which results in the most prominent resonances in the cavity. The highlighted d values in Table 3, which are calculated using m = 26, correspond to the peaks in Fig. 11. Even though the via heights 1.6 μm and 3.1 μm lead to higher coupling efficiency (80% and 75%, respectively), the via height 2 μm is chosen in consideration of fabrication feasibility and device performance. On one hand, it may be challenging to deposit more than 2 μm-thick Si via using conventional LPCVD without sacrificing deposition speed and layer uniformity. On the other hand, interlayer separations less than 2 μm may induce optical crosstalk between two layers, thus degrading the overall 3D interconnection. The case d = 2 μm has a longer coupling time (1.32 ps, temporal bandwidth δ_t = 0.76 THz) than d = 3.1 μm (0.83 ps, δ_t = 1.21 THz) due to a stronger resonance. Nevertheless, the GARC couplers would be fast enough to satisfy the terahertz communication requirements.

In the case of coupling between layers separated by an air gap, the GARC coupler could be divided into two parts for easier fabrication, one being the top waveguide and the via, the other being the bottom waveguide. Here we analyze the effect of vertical gaps between the two parts, assuming the via height is exactly 2 μm as designed. As shown in Fig. 12, the efficiency drops in an oscillating and exponentially decaying fashion. Since the power in the via is evanescently coupled to the bottom waveguide, it is expected that a large gap, e.g.

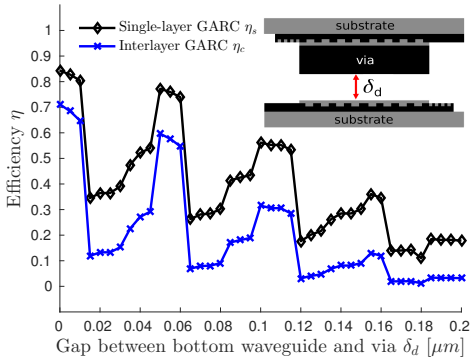

Fig. 12. Effect of vertical gap between via and bottom waveguide δ_d for the optimized Si/SiO_2 GARC coupler with target interlayer separation $d = 2\ \mu m$.

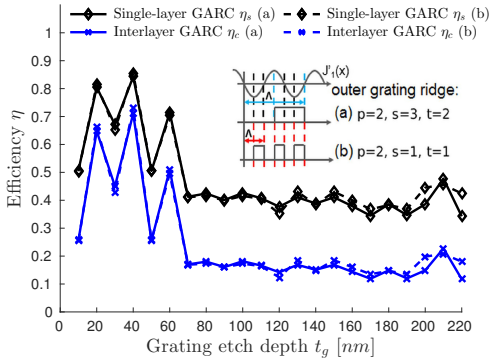

Fig. 14. Effect of grating etch depth t_g for the optimized Si/SiO_2 GARC coupler with $d = 2\ \mu m$. t_g indicates the etch depth for both the inner and outer circular gratings.

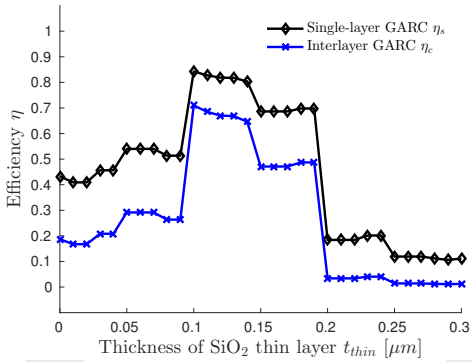

Fig. 13. Effect of SiO_2 thin layer thickness t_{thin} for the optimized Si/SiO_2 GARC coupler with $d = 2\ \mu m$.

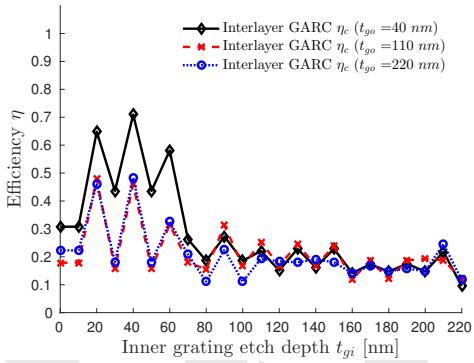

Fig. 15. Effect of varying the inner grating etch depth t_{gi} and the outer grating etch depth t_{go} for the optimized Si/SiO_2 GARC coupler with $d = 2\ \mu m$.

δ_d >200 nm, will prevent the coupling. For δ_d <200 nm, power can be coupled to the bottom waveguide but it is modulated by interference, just as in the cases of changing via height. From this analysis, we can see that the gap between layers of GARC coupler is detrimental to the coupling and it should be avoided. Therefore, ideally, the GARC structure should be grown layer by layer in a bottom-up approach.

Keeping the interlayer separation d at 2 μm, the effect of changing the thickness of the SiO_2 thin layer, t_{thin}, is shown in Fig. 13. The resonance in the via is weaker for smaller t_{thin}, while evanescent coupling is prohibited for larger t_{thin}, both resulting in lower coupling efficiency.

The effect of changing the grating etch depth t_g and changing the outer grating ridge definition (values of s and t) are also explored. As shown in Fig. 14, the efficiencies drop rapidly for $t_g > 80\ nm$ due to significant back-reflection from the circular grating into the input waveguide taper. The oscillations in the efficiencies are again due to interference effects (e.g. in the range $t_g \in [10, 80]\ nm$). The efficiency plots of the GARC coupler with $s = 3$ and $t = 2$ coincide with those of the GARC coupler with $s = 1$ and $t = 1$, which means that the two grating reflectors work equivalently. The values $s = 3$ and $t = 2$ are chosen because they result in wider grating ridges.

To reduce fabrication difficulty, the inner and outer grating etch depths are kept the same; that is, $t_{gi} = t_{go} = t_g$. For analysis purposes, varying the etch depths of the inner and outer grating separately offers a better understanding of the effects of circular gratings and the resonant cavity. Figure 15 shows the efficiency change with respect to the variation of inner grating etch depth t_{gi} for three outer grating etch depths $t_{go} = 40\ nm$, 110 nm, and 220 nm. At $t_{gi} = 0$, the inner circular grating is absent and the interlayer coupling efficiency is 20% to 30%. This is because the field in the inner circular slab waveguide, which is launched from the input taper, is not modulated and the field pattern is not symmetric about the circular waveguide center. As a result of the asymmetry, the field does not constructively interfere, even though the outer circular grating forms a resonant cavity. As the inner grating depth increases, the index contrast becomes larger, and so does the field modulation. The curves for the three outer grating depths have similar trends, but coupling losses are higher for larger t_{go} possibly due to stronger back-reflection. The highest coupling efficiency for the three cases $t_{go} = 40\ nm$, 110 nm, and 220 nm are all obtained at $t_{gi} = 40\ nm$. It can be concluded that, first, the shallow etch depth is necessary to achieve high coupling efficiency, and second, there is no benefit in defining different etch depths for the inner and outer circular gratings.

Furthermore, varying the grating ridge is another factor to consider. In the simulation, ridge locations with 4 decimal place

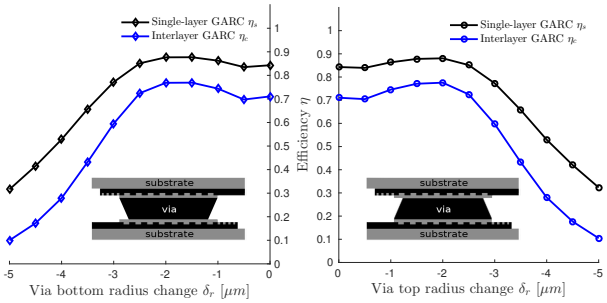

Fig. 16. Via tapering effect for the optimized Si/SiO_2 GARC coupler with $d = 2\ \mu m$.

accuracy are employed. However, it is not realistic to achieve such degree of accuracy in fabrication. Keeping the other parameters unchanged, we simulate a GARC coupler with a strictly periodic 0.55 μm inner grating ridge/groove width and 0.41 μm outer grating ridge/groove width, and the interlayer coupling efficiency is simulated as 65%, which is 4% smaller than the optimized GARC coupler specified in Table 2. This is due to the fact that the uniform inner grating doesn't follow the radial field distribution described by the 1st order Bessel function. Although it is common practice to use a strictly periodic grating, the Bessel-function-defined periods used here are shown to provide better performance.

Tapering effect of the via is also investigated. During the etching process, the side wall of the cylindrical via may not be exactly vertical. The effect of via radius change δ_r is shown in Fig. 16. Two scenarios are investigated: the via may be either tapering up or tapering down depending on the fabrication process. In either case, the narrow end of the via has a change of δ_r (a negative value) compared with the wide end whose radius is set as a fixed value $R = 7.0413\ \mu m$. The plots are symmetric about the axis at $\delta_r = 0$, which indicates a perfectly vertical side wall. This is reasonable because of the 180° rotational symmetry of the GARC structure and light reciprocity. The efficiencies exhibits moderate increase for $|\delta_r| < 2\ \mu m$ (28% change relative to R), which may due to a stronger field confinement at the narrow taper end. However, further radius decreases will violate the radial resonance condition in the via, thus inducing large coupling loss. As a result, tapering effect should be controlled within 2 μm radius deviations. Nevertheless, a tapering effect with more than 28% radius decrease is unlikely to occur.

Lastly, the GARC coupler is polarization dependent. The optimized GARC coupler for the TE polarization is not effective for coupling a TM polarized guided mode, and the coupling efficiency for TM polarization is $\eta_c = 20\%$. This is because the interference condition designed for the TE polarization doesn't satisfy the TM guided mode. On one hand, the radial propagation constants for the two polarizations are not the same, resulting different interference condition in the radial direction. On the other hand, the longitudinal propagation constants $\gamma_{Si} = \sqrt{k_0^2 n_{Si}^2 - \beta^2}$ are also different, causing different resonant conditions in the vertical cavity. Silicon exhibits a weak 2nd order nonlinearity $\chi^{(2)}$ due to its centrosymmetry diamond lattice, and most of its nonlinear effect comes from the 3rd order $\chi^{(3)}$, which is typically exploited using Si wires with small cross sections (<0.1 μm^2) [46]. Thus, the Si/SiO_2 GARC couplers with the optimized design are unlikely to be affected by the nonlinear effects.

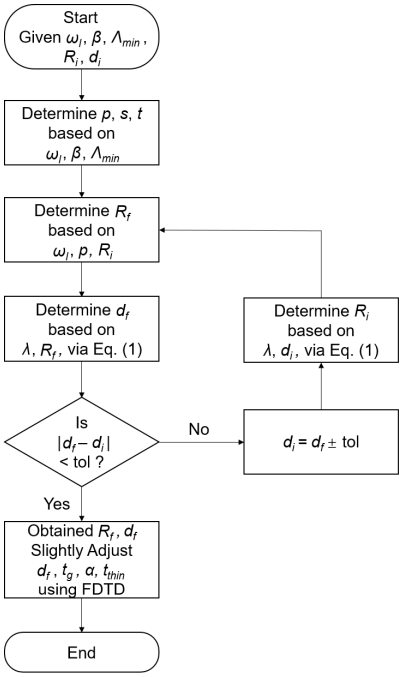

Fig. 17. Process flowchart for the design of GARC couplers that satisfies targeted interlayer distance d.

4. GARC COUPLER DESIGN FLOW

It is noted that the GARC coupler design provided in this paper is not the only high-efficiency design. By properly choosing the sizes of the resonant cavities, various interlayer distances d and coupler radii R can be achieved. A design flowchart is provided in Fig. 17 to accommodate various potential structure requirements. The zeros of Bessel function $J_1'(x)$ and the fundamental propagation constant β can be pre-calculated. Given the minimum grating period Λ_{min}, the parameters p, s, and t, which correspond to grating ridge widths, can be determined. The targeted interlayer distance and via radius are set as the initial values d_i and R_i, respectively. The updated values, d_f and R_f, will be determined by the initial values as well as by Eq. (1). The loop will be terminated if $|d_f - d_i| < tol$, where tol is the tolerance. If the via radius is more critical, the decision point should be $|R_f - R_i| < tol$ and the process can be accordingly modified. After d_f and R_f are obtained, FDTD can be used to finely tune the parameters (α, t_g, t_{thin}, and d_f) involved in the GARC model because the GARC coupler is more complex than a single cylindrical resonant cavity defined by Eq. (1).

5. DIFFERENCES BETWEEN THE GARC COUPLER AND FOCUSING GRATING COUPLERS

Focusing grating couplers, whose rulings are curved, have been reported to achieve efficient fiber-to-grating coupling [47–49]. These curved gratings, even though similar in shape to the circular gratings used in the GARC coupler, are based on a fundamentally different concept. The curved gratings are defined by the interference of two focusing beams (Beam 1 and 2) [47]. By directing Beam 1 toward the defined grating, Beam 2 can be

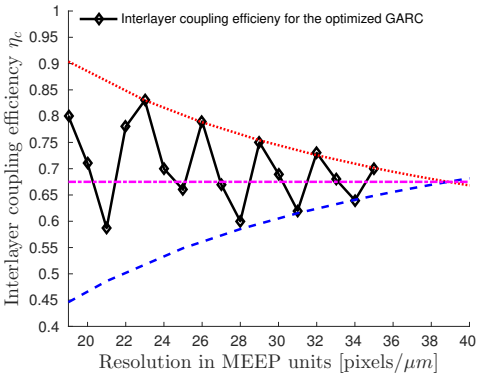

Fig. 18. Interlayer efficiency of GARC as a function of FDTD resolution. The approximately converged value is 68%.

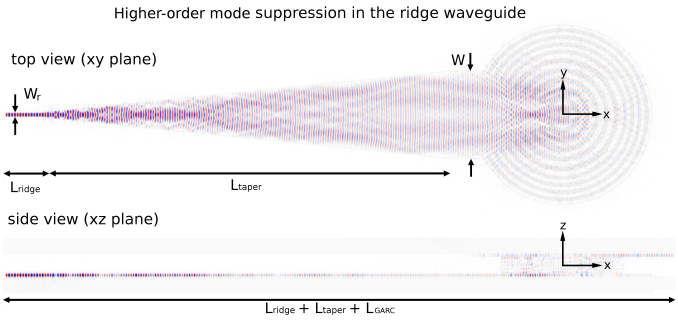

Fig. 19. A waveguide taper can be added to couple the GARC output slab waveguide to a ridge waveguide. Color is scaled based on the maximum power in the simulation.

generated, and vice versa. Similarly, the curved gratings used in [47, 49] are formed by the interference between an incident beam in the air, either a plane wave or a focusing beam, and a focusing wave in the waveguide. As a result, an externally incident wave, e.g. beam from the fiber, can excite the guided focusing wave, thus achieving the fiber-to-waveguide coupling. The focusing grating couplers defined by external and guided wave interference achieve fiber coupling to ridge waveguides. On the other hand, the circular gratings used in a GARC coupler are defined by an internal cylindrical wave front in the cylindrical cavity and no external beams are involved.

6. SUMMARY AND CONCLUSION

A vertical interlayer coupling structure (GARC) that uses circular gratings and a high-index via has been designed. A Si/SiO_2 GARC coupler is optimized to achieve 68% interlayer coupling efficiency (approximately 82% single-layer efficiency). The coupling structure is compact (20.72 μm), broad-band ($\delta_{\lambda,1dB}$ = 270 nm), and relatively straightforward to fabricate due to the wide grating ridges and the absence of adjacent-layer reflectors. The GARC coupler performance is less sensitive to variations in grating ridge width but it is more affected by the vertical layer thickness, e.g. grating etch depth and via height. However, compared with horizontal feature definition, vertical layer thicknesses are more easily controlled by regulating the deposition process. The GARC coupler is similar in principle to a Fabry–Perot resonator. Thus, it is conceivable for it to operate as an amplifier if it is doped with rare-earth element or to operate as a modulator together with electro-optic materials. Overall, the GARC structure represents a promising candidate for optically interconnecting layers in 2.5D and 3D IC technologies [1, 2].

7. APPENDIX

A. Effect of Resolution on Efficiency Calculations

Interlayer coupling efficiency of the GARC coupler was simulated using the MEEP 3D FDTD software package. This was done for a range of resolutions from 19 to 35 $pixels/\mu m$. From these calculations, the efficiency displayed an oscillating and converging trend, as shown in Fig. 18. This behavior is typical and due largely to the effects of the finite pixel size and the slight mismatches between the computational grid and the device structure. Subpixel-averaging, which is a process to assign carefully designed average values of the permittivity ϵ to pixels at the structural boundaries [50], may also occur to give more stable results. As seen from the figure, the efficiency at convergence is approximately 68%. According to [37], at least 8 pixels/wavelength in the highest dielectric should be used. The simulation results in the sensitivity analysis are obtained using the resolution 20 $pixels/\mu m$.

B. Higher-order Transverse Mode Suppression

If needed, higher-order modes in the GARC output slab waveguide can be suppressed by tapering the slab waveguide to a ridge waveguide. Figure 19 shows the simulation of the coupling of the GARC output field into a ridge waveguide (W_r = 0.5μm, L_{ridge} = 4 μm) using a taper (L_{taper} = 47.34 μm, half angle α_{taper} = 0.1 rad) to determine the coupling efficiency into only the fundamental mode of the ridge waveguide. In this case the interlayer coupling efficiency is 55%.

REFERENCES

1. "Integrated photonic systems roadmap international (IPSR-I)," http://photonicsmanufacturing.org.
2. M. Glick, L. C. Kimmerling, and R. C. Pfahl, "A roadmap for integrated photonics," Opt. Photon. News **29**, 36 (2018).
3. K. Puttaswamy and G. H. Loh, "Thermal herding: Microarchitecture techniques for controlling hotspots in high-performance 3D-integrated processors," in "IEEE 13th International Symposium on High Performance Computer Architecture," (IEEE, 2007), pp. 193–204.
4. K. W. Lee, T. Nakamura, K. Sakuma, K. T. Park, H. Shimazutsu, N. Miyakawa, K. Y. Kim, H. Kurino, and M. Koyanagi, "Development of three-dimensional integration technology for highly parallel image-processing chip," Jpn. J. Appl. Phys. **39**, 2473 (2000).
5. A. Osseiran, F. Boccardi, V. Braun, K. Kusume, P. Marsch, M. Maternia, O. Queseth, M. Schellmann, H. Schotten, H. Taoka, H. Tulberg, M. A. Uusitalo, B. Timus, and M. Fallgren, "Scenarios for 5G mobile and wireless communications: the vision of the METIS project," IEEE Commun. Mag. **52**, 26–35 (2014).
6. N. Sherwood-Droz and M. Lipson, "Scalable 3D dense integration of photonics on bulk silicon," Opt. Express **19**, 17758–17765 (2011).
7. C. Wan, T. K. Gaylord, and M. S. Bakir, "Grating design for interlayer optical interconnection of in-plane waveguides," Appl. Opt. **55**, 2601–2610 (2016).
8. G. Roelkens, D. Vermeulen, D. Van Thourhout, R. Baets, S. Brision, P. Lyan, P. Gautier, and J.-M. Fedeli, "High efficiency diffractive grating couplers for interfacing a single mode optical fiber with a nanophotonic silicon-on-insulator waveguide circuit," Appl. Phys. Lett. **92**, 131101 (2008).
9. G. Roelkens, D. Van Thourhout, and R. Baets, "High efficiency silicon-

on-insulator grating coupler based on a poly-silicon overlay," Opt. Express **14**, 11622–11630 (2006).
10. D. Vermeulen, S. Selvaraja, P. Verheyen, G. Lepage, W. Bogaerts, P. Absil, D. Van Thourhout, and G. Roelkens, "High-efficiency fiber-to-chip grating couplers realized using an advanced cmos-compatible silicon-on-insulator platform," Opt. Express **18**, 18278–18283 (2010).
11. C. Wan, T. K. Gaylord, and M. S. Bakir, "RCWA-EIS method for interlayer grating coupling," Appl. Opt. **55**, 5900–5908 (2016).
12. G. Roelkens, D. Vermeulen, S. Selvaraja, R. Halir, W. Bogaerts, and D. Van Thourhout, "Grating-based optical fiber interfaces for silicon-on-insulator photonic integrated circuits," IEEE J. Sel. Top. Quantum Electron. **17**, 571–580 (2011).
13. S. K. Selvaraja, D. Vermeulen, M. Schaekers, E. Sleeckx, W. Bogaerts, G. Roelkens, P. Dumon, D. Van Thourhout, and R. Baets, "Highly efficient grating coupler between optical fiber and silicon photonic circuit," in "Conf. Lasers Electro-Optics," (Optical Society of America, 2009), p. CTuC6.
14. D. Taillaert, P. Bienstman, and R. Baets, "Compact efficient broadband grating coupler for silicon-on-insulator waveguides," Opt. Lett. **29**, 2749–2751 (2004).
15. D. Taillaert, F. Van Laere, M. Ayre, W. Bogaerts, D. Van Thourhout, P. Bienstman, and R. Baets, "Grating couplers for coupling between optical fibers and nanophotonic waveguides," Jpn. J. Appl. Phys. **45**, 6071–6077 (2006).
16. J. H. Kang, Y. Atsumi, Y. Hayashi, J. Suzuki, Y. Kuno, T. Amemiya, N. Nishiyama, and S. Arai, "50 Gbps data transmission through amorphous silicon interlayer grating couplers with metal mirrors," Appl. Phys. Express **7**, 032202 (2014).
17. X. Chen, C. Li, C. K. Fung, S. M. Lo, and H. K. Tsang, "Apodized waveguide grating couplers for efficient coupling to optical fibers," IEEE Photon. Technol. Lett. **22**, 1156–1158 (2010).
18. D. Taillaert, W. Bogaerts, P. Bienstman, T. F. Krauss, P. V. Daele, I. Moerman, S. Verstuyft, K. D. Mesel, and R. Baets, "An out-of-plane grating coupler for efficient butt-coupling between compact planar waveguides and single-mode fibers," IEEE J. Quantum Electron. **38**, 949–955 (2002).
19. H. L. Tseng, E. Chen, H. Rong, and N. Na, "High-performance silicon-on-insulator grating coupler with completely vertical emission," Opt. Express **23**, 24433–24439 (2015).
20. M. Dai, L. Ma, Y. Xu, M. Lu, X. Liu, and Y. Chen, "Highly efficient and perfectly vertical chip-to-fiber dual-layer grating coupler," Opt. Express **23**, 1691–1698 (2015).
21. J. Notaros, F. Pavanello, M. T. Wade, C. M. Gentry, A. Atabaki, L. Alloatti, R. J. Ram, and M. A. Popović, "Ultra-efficient CMOS fiber-to-chip grating couplers," in "Optical Fiber Commun. Conf.", (IEEE, 2016), pp. 1–3.
22. X. Chen, D. J. Thomson, L. Crudginton, A. Z. Khokhar, and G. T. Reed, "Dual-etch apodised grating couplers for efficient fibre-chip coupling near 1310 nm wavelength," Opt. Express **25**, 17864–17871 (2017).
23. D. Benedikovic, C. Alonso-Ramos, P. Cheben, J. H. Schmid, S. Wang, D.-X. Xu, J. Lapointe, S. Janz, R. Halir, A. Ortega-Moñux, J. Fedeli, S. Janz, I. Molina-Fernandez, and M. Dado, "High-directionality fiber-chip grating coupler with interleaved trenches and subwavelength index-matching structure," Opt. Lett. **40**, 4190–4193 (2015).
24. T. Watanabe, M. Ayata, U. Koch, Y. Fedoryshyn, and J. Leuthold, "Perpendicular grating coupler based on a blazed antiback-reflection structure," IEEE J. Light. Technol. **35**, 4663–4669 (2017).
25. L. Liu, M. Pu, K. Yvind, and J. M. Hvam, "High-efficiency, large-bandwidth silicon-on-insulator grating coupler based on a fully-etched photonic crystal structure," Appl. Phys. Lett. **96**, 051126 (2010).
26. Q. Zhong, V. Veerasubramanian, Y. Wang, W. Shi, D. Patel, S. Ghosh, A. Samani, L. Chrostowski, R. Bojko, and D. V. Plant, "Focusing-curved subwavelength grating couplers for ultra-broadband silicon photonics optical interfaces," Opt. Express **22**, 18224–18231 (2014).
27. L. Yu, L. Liu, Z. Zhou, and X. Wang, "High efficiency binary blazed grating coupler for perfectly-vertical and near-vertical coupling in chip level optical interconnections," Opt. Commun. **355**, 161–166 (2015).
28. B. Wohlfeil, L. Zimmermann, and K. Petermann, "Optimization of fiber grating couplers on SOI using advanced search algorithms," Opt. Lett. **39**, 3201–3203 (2014).
29. C. Wan, T. K. Gaylord, and M. S. Bakir, "Rigorous coupled-wave analysis equivalent-index-slab method for analyzing 3D angular misalignment in interlayer grating couplers," Appl. Opt. **55**, 10006–10015 (2016).
30. C. Wan, T. K. Gaylord, and M. S. Bakir, "Circular waveguide grating-via-grating for interlayer coupling," IEEE Photon. Technol. Lett. **29**, 1776–1779 (2017).
31. J. Bolten, J. Hofrichter, N. Moll, S. Schönenberger, F. Horst, B. J. Offrein, T. Wahlbrink, T. Mollenhauer, and H. Kurz, "CMOS compatible cost-efficient fabrication of SOI grating couplers," Microelectron. Eng. **86**, 1114–1116 (2009).
32. B. Schmid, A. Petrov, and M. Eich, "Optimized grating coupler with fully etched slots," Opt. Express **17**, 11066–11076 (2009).
33. S. Bernabé, C. Kopp, M. Volpert, J. Harduin, J.-M. Fédéli, and H. Ribot, "Chip-to-chip optical interconnections between stacked self-aligned SOI photonic chips," Opt. Express **20**, 7886–7894 (2012).
34. S. Lardenois, D. Pascal, L. Vivien, E. Cassan, S. Laval, R. Orobtchouk, M. Heitzmann, N. Bouzaida, and L. Mollard, "Low-loss submicrometer silicon-on-insulator rib waveguides and corner mirrors," Opt. Lett. **28**, 1150–1152 (2003).
35. M. Antelius, K. B. Gylfason, and H. Sohlström, "An apodized SOI waveguide-to-fiber surface grating coupler for single lithography silicon photonics," Opt. Express **19**, 3592–3598 (2011).
36. Y. Tang, Z. Wang, L. Wosinski, U. Westergren, and S. He, "Highly efficient nonuniform grating coupler for silicon-on-insulator nanophotonic circuits," Opt. Lett. **35**, 1290–1292 (2010).
37. "MEEP tutorial," http://ab-initio.mit.edu/wiki/index.php/Meep_Tutorial.
38. M. Toda, "Single-mode behavior of a circular grating for potential disk-shaped DFB lasers," IEEE J. Quantum Electron. **26**, 473–481 (1990).
39. R. M. Schimpe, "Cylindrical diffraction grating couplers and distributed feedback resonators for guided wave devices," U.S. patent 4,743,083, issued May 10, 1988 .
40. E. Ben-Bassat and J. Scheuer, "Optimal design of radial Bragg cavities and lasers," Opt. Lett. **40**, 3069–3072 (2015).
41. X. Li and S. Yu, "Static and dynamic modeling of circular grating-coupled distributed feedback lasers," IEEE J. Quantum Electron. **44**, 770–776 (2008).
42. X. Gong, A. Chan, and H. Taylor, "Lateral mode discrimination in surface emitting DBR lasers with cylindrical symmetry," IEEE J. Quantum Electron. **30**, 1212–1218 (1994).
43. F. Van Laere, G. Roelkens, M. Ayre, J. Schrauwen, D. Taillaert, D. Van Thourhout, T. F. Krauss, and R. Baets, "Compact and highly efficient grating couplers between optical fiber and nanophotonic waveguides," IEEE J. Light. Technol. **25**, 151–156 (2007).
44. J. Yao, X. Zheng, G. Li, I. Shubin, H. Thacker, Y. Luo, K. Raj, J. E. Cunningham, and A. V. Krishnamoorthy, "Grating-coupler based low-loss optical interlayer coupling," in "8th IEEE Intl. Conf. Group IV Photon.", (2011), pp. 383–385.
45. D. M. Pozar, "Circular waveguide cavity resonators," in "Microwave Engineering," (Wiley, 2011), chap. 6.4, pp. 288–292.
46. J. Leuthold, C. Koos, and W. Freude, "Nonlinear silicon photonics," Nat. Photonics **4**, 535 (2010).
47. D. Heitmann and C. Ortiz, "Calculation and experimental verification of two-dimensional focusing grating couplers," IEEE J. Quantum Electron. **17**, 1257–1263 (1981).
48. V. A. Kiselev and S. N. Shaposhnikov, "Wide-aperture focusing in the case of excitation of an optical waveguide through an annular grating," Sov. Phys. Tech. Phys. **33**, 987–989 (1988).
49. F. Van Laere, T. Claes, J. Schrauwen, S. Scheerlinck, W. Bogaerts, D. Taillaert, L. O'Faolain, D. Van Thourhout, and R. Baets, "Compact focusing grating couplers for silicon-on-insulator integrated circuits," IEEE Photon. Technol. Lett. **19**, 1919–1921 (2007).
50. A. F. Oskooi, D. Roundy, M. Ibanescu, P. Bermel, J. D. Joannopoulos, and S. G. Johnson, "MEEP: A flexible free-software package for electromagnetic simulations by the FDTD method," Comput. Phys. Commun. **181**, 687–702 (2010).